

## Research Paper

# A study on particle breakage behavior during pile penetration process using acoustic emission source location

Wuwei Mao <sup>a,b,\*</sup>, Shogo Aoyama <sup>c</sup>, Ikuo Towhata <sup>d</sup>

<sup>a</sup> Department of Geotechnical Engineering, College of Civil Engineering, Tongji University, Shanghai 200092, China

<sup>b</sup> Key Laboratory of Geotechnical and Underground Engineering, Ministry of Education, Tongji University, Shanghai 200092, China

<sup>c</sup> Kiso - Jiban Consultants Co., Ltd., Tokyo, Japan

<sup>d</sup> Department of Civil Engineering, University of Tokyo, Tokyo, Japan



## ARTICLE INFO

### Article history:

Received 21 July 2018

Received in revised form

17 December 2018

Accepted 3 April 2019

Available online 18 April 2019

### Keywords:

Acoustic emission

Source location

Sand

Particle breakage

Pile

## ABSTRACT

Particle breakage is a common occurrence in granular systems when the external stress exceeds the individual particle strength. A large number of experimental evidences suggested that particle breakage may significantly influence the soil behavior. In the case of pile foundations, the subsoil below the pile tip experiences considerable high stress and consequently prone to break. Due to the lack of sufficient understanding on particle breakage mechanism, there is currently no simultaneous theoretical background for particle breakage analysis during the pile penetration process. This study aims to clarify the location of particle breakage and its evolving characteristics with the aid of acoustic emission (AE) source location method. The spatial distribution of AE hypocenters is interpreted to be associated with the mechanism of particle breakage. Results showed that the AE sources were not uniformly distributed, but concentrated within certain zones below the pile tip. This AE concentration zone was pushed downward with the advancing pile tip, and its distance from the real time pile tip position decreased after certain depth of pile penetration. The location of particle breakage interpreted from AE source location was verified with posttest excavations and the insights on the particle breakage evolution zone were further discussed.

© 2019, China University of Geosciences (Beijing) and Peking University. Production and hosting by Elsevier B.V. This is an open access article under the CC BY-NC-ND license (<http://creativecommons.org/licenses/by-nc-nd/4.0/>).

## 1. Introduction

The mechanical property of highly stressed soils is one of the fundamental concerns in soil mechanics. Individual particles are prone to breakage when the external stresses exceed their strengths, which may eventually influence the strength and relevant mechanical characteristics of the soil mass. The phenomenon of particle breakage and its resultant effect on soil behavior has been comprehensively investigated by a large number of previous studies (Ueng and Chen, 2000; Sadrekarimi and Olson, 2010; Bandini and Coop, 2011; Ghafghazi et al., 2014; Xiao et al., 2015a, b, 2017, 2018a; Yu, 2017a, b, c). Constitutive models incorporated with particle breakage for better interpretation of the mechanical characteristics of soils subjected to particle degradation have also been

proposed (Salim and Indraratna, 2004; Einav, 2007; Indraratna et al., 2007; Hu et al., 2011; Xiao and Liu, 2017; Xiao et al., 2018b).

In the field of geotechnical engineering, particle breakage is involved in various engineering processes, e.g. the footing of large dams or embankments (Sadrekarimi, 2012), and soils around the pile tip (Yasufuku and Hyde, 1995; Jardine et al., 2013a, b), or natural hazard processes, e.g. particle fragmentation during rockslides (Imre et al., 2010). In the case of pile foundations, a variety of laboratory and field tests are nowadays in practice for characterization of the pile behavior (Randolph, 2003; Yang, 2006; Jardine et al., 2013a, b). In particular, more and more studies are paying attention to the stress/strain characteristics of the end bearing area of the pile. Novel experimental approaches such as multiple stress sensor array, tactile pressure sensing array, X-ray CT, or the digital image correlation technique have been applied for investigation of stress/strain behaviors around a pile tip (White and Bolton, 2004; Eskişar et al., 2012; Jardine et al., 2013a; Aoyama et al., 2016). These efforts have substantially improved scientific understandings on the pile behavior. Meanwhile, the significance of particle

\* Corresponding author. Department of Geotechnical Engineering, College of Civil Engineering, Tongji University, Shanghai 200092, China.

E-mail address: [maowuwei@tongji.edu.cn](mailto:maowuwei@tongji.edu.cn) (W. Mao).

Peer-review under responsibility of China University of Geosciences (Beijing).

breakage below the pile tip has been well recognized through close-up observations as well (McDowell and Bolton, 2000; White and Bolton, 2004; Kuwajima et al., 2009; Yang et al., 2010; Altuhafi et al., 2017). Generally speaking, lower bearing capacity is expected for ground subjected to considerable particle breakage based on field and laboratory measurements (Murff, 1987; Kuwajima et al., 2009). Although different approaches have been proposed for the evaluation of ground bearing capacity considering particle breakage, the theoretical backgrounds and their assumptions vary widely, such as the spherical cavity expansion method proposed by Yasufuku and Hyde (1995), the constant relative breakage surface method proposed by Simonini (1996), the DEM analysis performed by Lobo-Guerrero and Vallejo (2005), and the breakage mechanics theory developed by Einav (2007) and Zhang et al. (2013, 2014). So far, there is still lack of consensus on the analysis of particle breakage problem under pile load. Further insights on the related issues are yet to be achieved. The most fundamental concerns include the exact location of particle breakage and how does it evolves with the advancing pile.

Regarding experimental approaches, the commonly used method for particle breakage assessment is the posttest excavation and measurement of grain size distribution (GSD). Based on the above mentioned approaches, however, the insights into the particle breakage are limited to the posttest characteristics, while the associated characteristics during the corresponding process remain unknown.

Distinct from the previous studies, this study focuses on the micro-scale energy dissipations in the form of elastic waves originating from the stressed sands subjected to pile loading. The elastic waves released from stressed materials, also known as acoustic emission (AE), have been widely adopted for investigating the failure process of various types of materials (Shiotani, 2006; Al-Balushi et al., 2010; He et al., 2010; Gutkin et al., 2011; Filippov et al., 2017). As part of the irrecoverable energy dissipations due to the plastic straining of the stressed material, AE is deemed to be highly associated with the material's failure mechanism. Previous studies on AE monitoring of pile penetration process suggested that the intensity of AE activity corresponded well with the ground bearing behavior (Mao et al., 2015, 2018a, b). Apart from the AE signal intensity, it is expected that the positions of the active AE should be associated with locations of the severest stress concentration or strain mobilization, which could provide potential insights into the spatial locations of particle breakage. Up to now, the AE source location has been successfully used for defect localization of many different materials, such as crack growth study of steels (Roberts and Talebzadeh, 2003), damage diagnosis of concretes (Carpinteri et al., 2007) and leakage detection of pipes (Butterfield et al., 2017). The spatial distribution of AE hypocenters can provide direct insights into their source regions, which is relatively difficult to be uncovered through traditional measurements. Therefore, the idea to study the particle breakage behavior by analyzing of AE source location is proposed. To implement this idea, an AE source location testing approach was firstly developed based on the framework of multi-sensor array positioning. Further, model pile penetration test was conducted to explore the subsoil behavior subjected to pile penetration with AE instrumentation. At last, the region of particle breakage interpreted from AE source location was verified with posttest excavations and the insights on the particle breakage evolution zone were discussed.

## 2. Experimental details

### 2.1. Model setup

**Fig. 1** shows the overview of the soil tank designed for the pile loading test. The internal dimension of the soil tank was 1600 mm

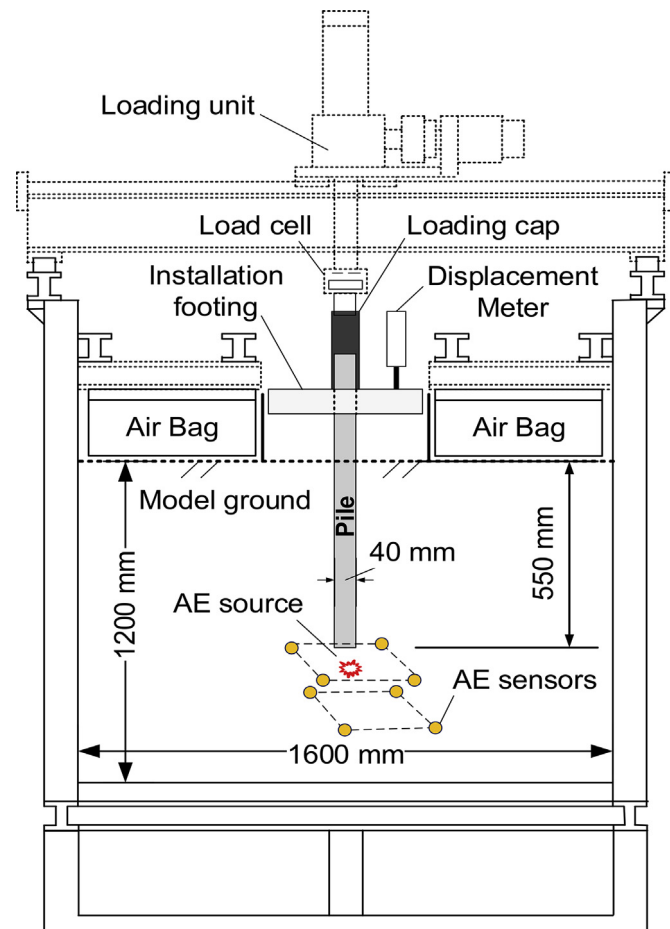


**Fig. 1.** Schematic illustration of the pile loading system.

in length, 1600 mm in width and 1680 mm in height. The loading unit was electric servo controlled and its location was movable within the frame plane. The maximum capacity of the loading unit was 500 kN with adjustable loading speed ranging from 0.1 to 10 mm/min. The load applied on the pile cap was measured by a load cell installed together with the loading head. The pile settlement was measured by a displacement transducer. Air bags were used to apply the surcharge on the ground surface. The compressed air was supplied to the air bags by a gas compressor. The surcharge pressure applied by air bags was monitored by a pressure gauge and can be adjusted to the target value through a control valve. The end-closed model pile had an outer diameter ( $D$ ) of 40 mm, thickness of 4 mm and length of 1000 mm. Strain gauges were pasted near the pile tip to measure the pile tip resistance as shown in **Fig. 2**. In the present study, the loading speed and the surcharge pressure were set at 0.5 mm/min and 100 kPa respectively.

### 2.2. Material and model ground setup

The materials commonly used for laboratory investigation of the particle breakage problem are the silica sand and the carbonate sand (Yasufuku and Hyde, 1995; McDowell and Bolton, 2000; Kuwajima et al., 2009; Yang et al., 2010; Zhang et al., 2013; Yu, 2017a, b, c). A previous study suggested that the stressed silica sand may produce much significant AE signals (Mao et al., 2018b), which is a crucial advantage for AE source location. Therefore, silica sand was adopted in this study for model ground preparation. The basic properties of the sand are shown in **Table 1**, and the grain size

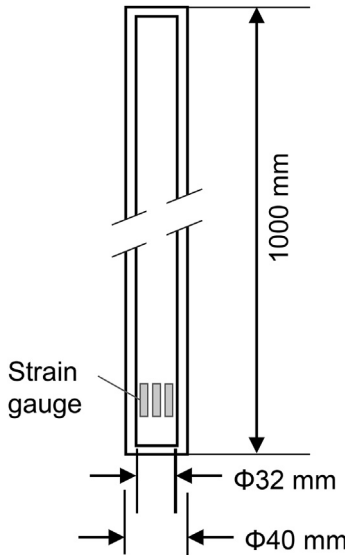


**Fig. 2.** Model pile and the positions of strain gauges.

distribution obtained by the sieve analysis is presented in Fig. 3. The mean diameter of the sand is 0.32 mm, while the maximum diameter is supposed to be less than 0.6 mm since all sands passed through the sieve with 0.6 mm aperture width as shown in Fig. 3.

The model ground was built layer by layer (150 mm each layer) through air pluviation, and then further compacted to reach the desired density. The relative density computed from the sand weight and the total volume measured around 85%. The final height of the model ground was 1200 mm. The initial embedded depth of the model pile was 550 mm (13.75D, D refers to the pile diameter) to the surface of the model ground and 650 mm (16.25D) to the base of the soil tank.

### 3. Acoustic emission source location

#### 3.1. Sensor array arrangement

Fig. 4 shows a typical configuration of the subsoil after pile penetration observed by posttest excavation (Aoyama et al., 2016). It is seen that the most affected area was limited within a half-sphere shaped region below the pile tip. Such failure pattern was also observed in previous studies (Yasufuku and Hyde, 1995; Yasufuku et al., 2001; Kuwajima et al., 2009). Therefore, the target area for AE localization is aimed at the above region. Meanwhile, considering the property of wave attenuation during propagation from source to the sensors, it is necessary to place the

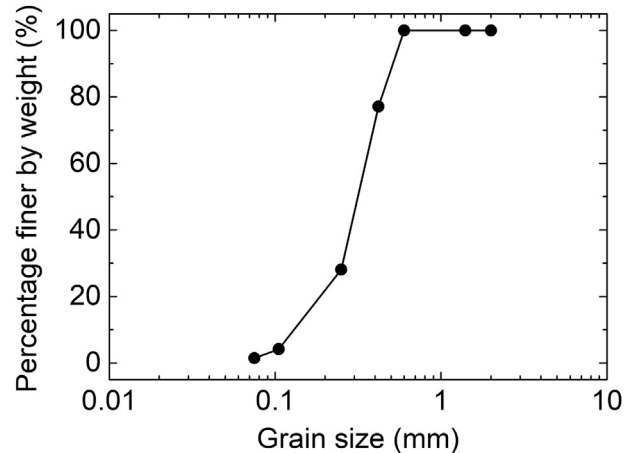


**Fig. 3.** Grain size distribution of the tested sand.

sensor not too far away from the potential AE source region so that the onset of the event signals from far side can also be successfully identified.

In the current study, eight sensors, model VS-BV201, manufactured by NEC/TOKIN Corporation, Japan, were used and all the sensors were embedded directly in sand near the pile tip. The position of each sensor was predetermined. After the model ground was filled to the desired level, the sensors were placed properly before filling the next layer of sand. The exact position of sensor was adjusted by its distance to the sidewall and the top of the soil tank. In general, all eight sensors were set at two levels, which were 10 and 90 mm below the initial pile end respectively. Horizontal distance between the sensor and pile center was set as 70 mm. Posttest excavations confirmed that the positions of the sensors were not affected by the penetration process of the pile. The detailed positions of the sensor arrangement are schematically illustrated in Fig. 5 and the coordinates of the sensors are summarized in Table 2. In such case, the potential locations of AE source below the pile tip were surrounded by the AE sensor array.

#### 3.2. Location of AE events

The AE signals detected by the sensors were digitalized continuously with a sampling rate of 500k samples/second through a high speed data logger. In a Cartesian coordinate system, the



**Fig. 4.** Typical subsoil configuration below a pile tip after penetration (after Aoyama et al., 2016).

**Table 1**  
Properties of the tested silica sand.

Property	Index
Specific gravity ( $G_s$ )	2.65
Maximum void ratio ( $e_{max}$ )	1.06
Minimum void ratio ( $e_{min}$ )	0.65
<sup>a</sup> Particle size ( $D_{10}$ , mm)	0.13
<sup>a</sup> Particle size ( $D_{30}$ , mm)	0.26
<sup>a</sup> Particle size ( $D_{50}$ , mm)	0.32
<sup>a</sup> Particle size ( $D_{60}$ , mm)	0.35
Coefficient of uniformity ( $C_u$ )	2.69
Coefficient of curvature ( $C_c$ )	1.48
Relative density ( $D_r$ )	85%

<sup>a</sup> D-values represent the diameters of the sand particles at the intercepts for 10%, 30%, 50%, 60% of the cumulative sand mass.

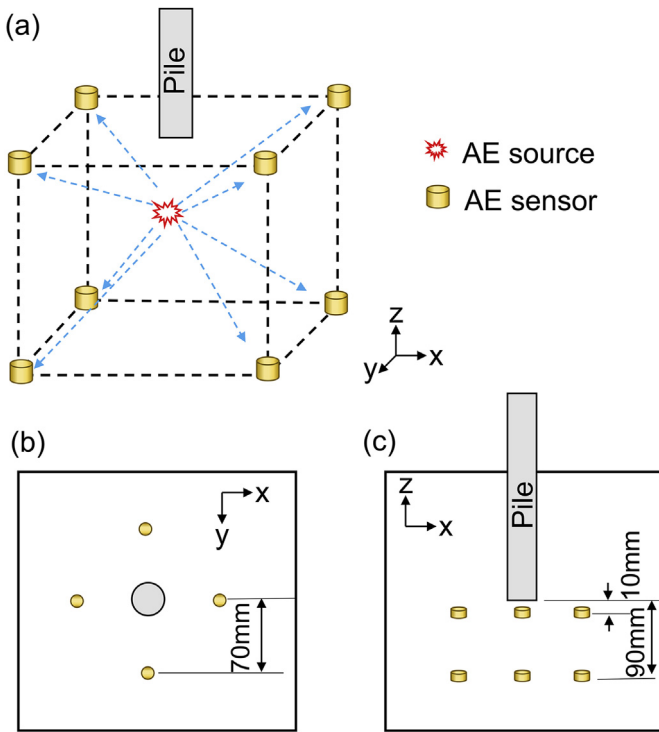


**Fig. 5.** Layout of the sensor arrangement. (a) 3D view; (b) top view; (c) front view.

distance between the AE sensors and a specific AE event can be determined as following (Kundu, 2014):

$$d_i = \sqrt{(x_0 - x_i)^2 + (y_0 - y_i)^2 + (z_0 - z_i)^2} = v \times (t_i - t_0) \quad (1)$$

where  $x_0, y_0, z_0$  are the coordinates of the unknown AE event source locations,  $v$  is the wave velocity,  $t_0$  is the source time,  $t_i, x_i, y_i, z_i$  ( $i = 1, 2, 3, \dots$ ) are the detected arrival time by each sensor and the predetermined coordinates of the AE sensors, respectively. By assuming a constant wave velocity, there are only four unknowns in Eq. (1). Theoretically, a four-sensor array would be possible to localize one AE event based on the Time Difference of Arrival (TDOA) among sensors (Kundu, 2014; Dong et al., 2015). In practice, more sensors are usually arranged in order to eliminate the potential errors.

In Eq. (1), the positions of the AE sensors can be determined during the experimental setup. Therefore, reliable signal source location requires accurate determination of the arrival times picked by each sensor. Considering huge number of individual events are expected to be detected during the pile loading process (Mao et al., 2015), an automatic arrival time determination algorithm based on

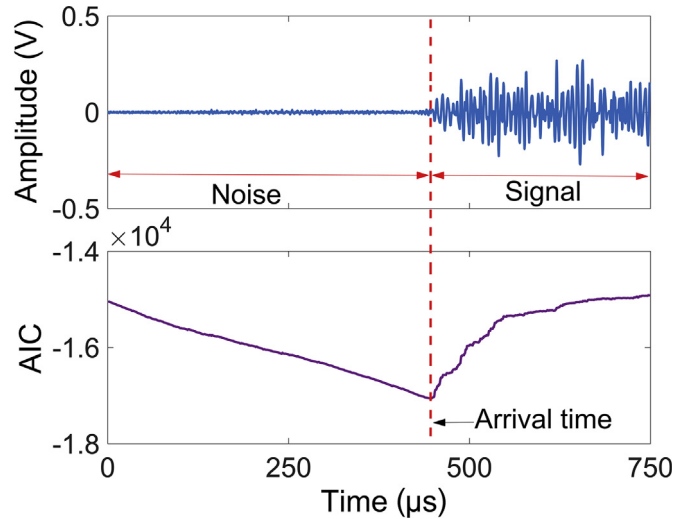


**Fig. 6.** Illustration of a typical wave signal and the performance of the AR-AIC method for arrival time determination of the signal.

Autoregressive-Akaike Information Criteria (AR-AIC) is developed. In the AR-AIC model, the non-stationary AE signals are described as locally stationary AR processes within each time window (Takanami and Kitagawa, 1988; Niccolini et al., 2012). Then, each time window is divided into two segments, which are assumed to be the noise part and the signal part. The dividing point is subsequently moved to the next point after the AIC value is computed at the current point, and the arrival of the signal corresponds to the minimum AIC value within the whole time window according to the Akaike Information Criteria (Akaike, 1973). An example of the AE signal and the performance of the AR-AIC model is illustrated in Fig. 6.

Verification tests with known signal locations were also performed to evaluate the accuracy of the source location method developed in this study. It is generally found that more than 90% of the predicted sources were located within the 15 mm distance to their true positions. Such accuracy is comparable with those AE source location studies on rock or composite materials (Eaton et al., 2012; Huang et al., 2013).

#### 4. Analysis of AE source location results

Two loading cycles, i.e. initial loading (1st loading) and followed by reloading (2nd loading), were conducted and the penetration depth of each loading was 20 mm. Detailed results of AE source location are displayed with every 2 mm (0.05D) penetration interval in Figs. 7 and 8 respectively. The whole plot covers an area of 2D in width and 4D in height, and is divided into  $40 \times 80$  sub-patches. The density distributions of the AE source are represented by the percentage ( $P$ ) of source event number falling within each patch.

In general, the AE sources were concentrated within the area at certain depth below the pile tip, rather than uniformly distributed, which also indicated the localized zone of particle breakage. The overall shape of the AE source distribution at different penetration depths had similar appearance. That is, the maximum distribution density zone located at certain depth below the pile tip, and it reduced with a radial gradient in all directions. One exception is that, during the first 2 mm penetration of the initial loading as shown in Fig. 7, the AE sources were relatively randomly distributed. As the penetration proceeded, more AE events were found to be clustered together. On the other hand, during the reloading

**Table 2**  
The coordinates of the sensor array.

Sensor No.	Coordinate (m)		
	x	y	z
S1	0	0.07	-0.09
S2	0.07	0	-0.09
S3	0	-0.07	-0.09
S4	-0.07	0	-0.09
S5	0	0.07	-0.01
S6	0.07	0	-0.01
S7	0	-0.07	-0.01
S8	-0.07	0	-0.01

<sup>a</sup> The origin of coordinates was set at the center of pile end before loading.

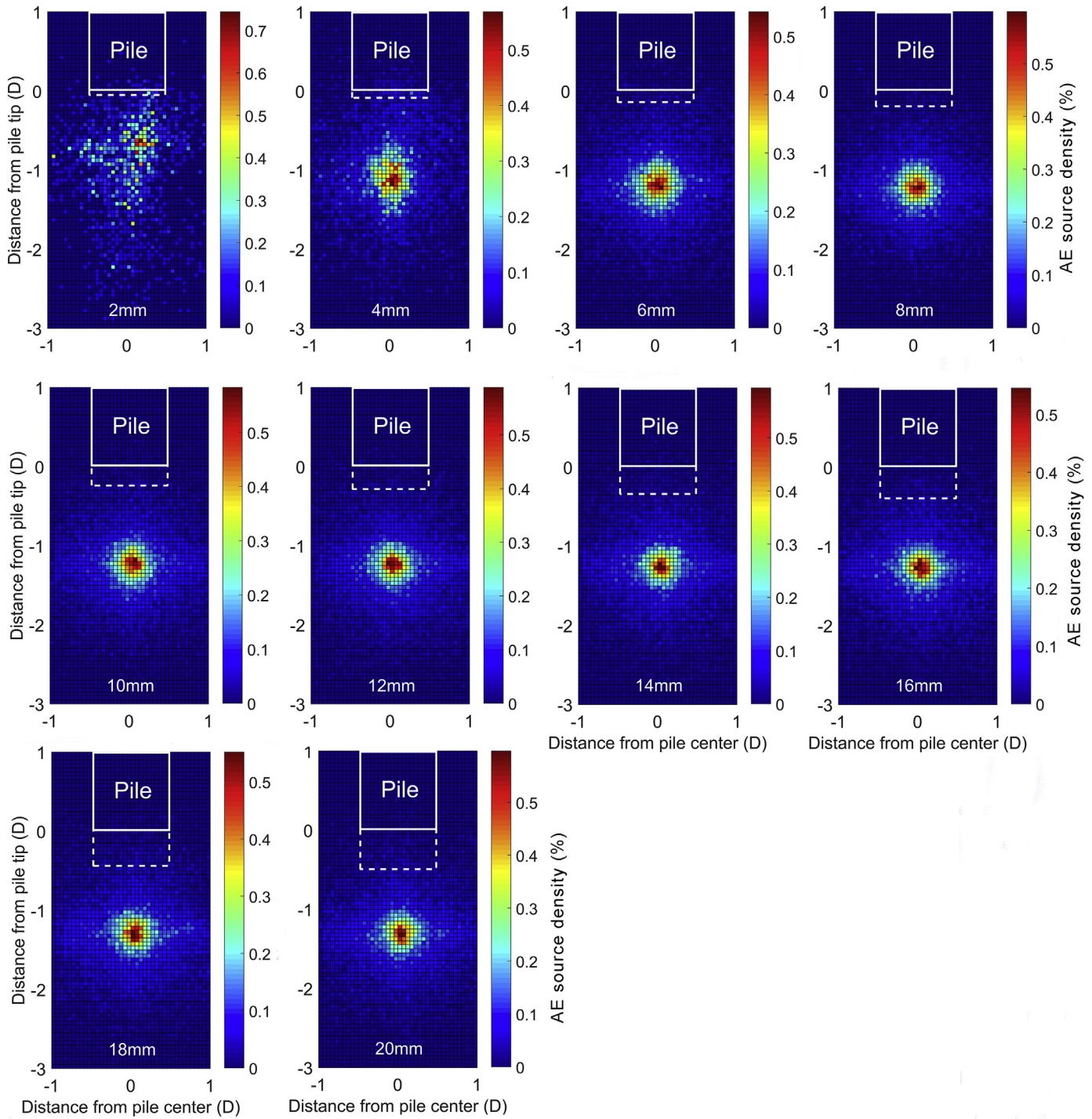


**Fig. 7.** Spatial distribution of AE source: 1st load.

process as shown in Fig. 8, the AE source distributions were relatively concentrated even for the first 2 mm penetration. This is because after the initial loading, the soil fabric was already formed below the pile tip. Therefore, the pattern of AE source distribution was similar with the prior loading stage (i.e. 20 mm during the initial loading).

The contour plots shown in Figs. 9 and 10 quantitatively display the source distributions with the origin of coordinate in the depth direction modified as the real time position of the pile tip. A

noticeable feature from these figures is that the AE source distribution, except for the first 2 mm penetration period, showed concentric circle diffusion and the center part was most active. In order to further assess the AE source distribution along the depth direction, the data of the profile along the pile center was retrieved and displayed in Fig. 11. During the 1st loading, the AE source was not noticeable until the ground depth reached around 0.5D below the pile tip. While during the 2nd loading, this value became about 1D. It seems that the zone of AE source concentration was pushed

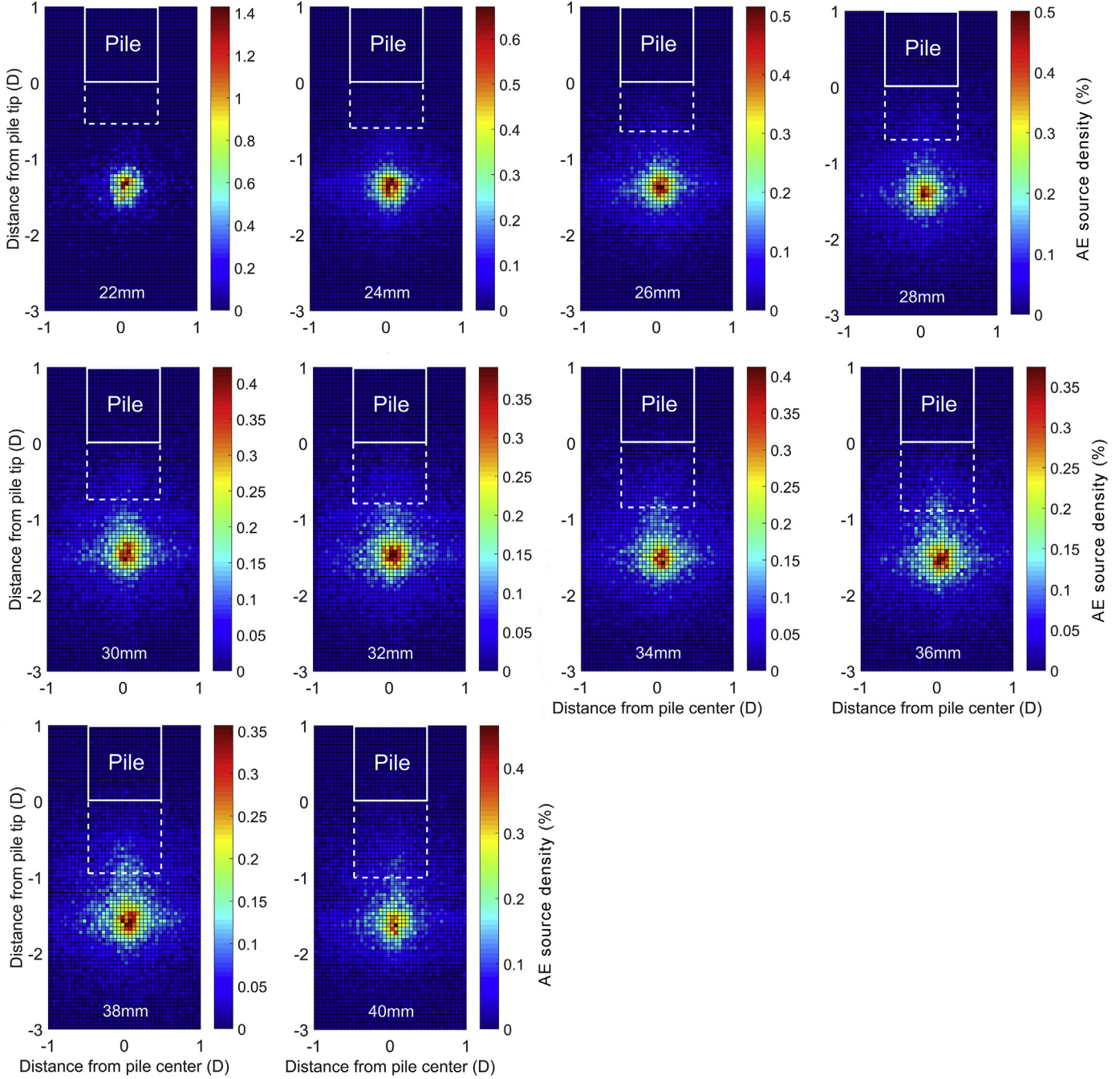


**Fig. 8.** Spatial distribution of AE source: 2nd load.

downward together with the advancing pile tip. This trend is more noticeable when the relative distance between the AE source and the real time pile end position is directly displayed, as shown in Fig. 12. The origin of the axis in the depth direction is subjected to change and is set to be the same with the real time pile tip position when the pile was penetrating downward (Fig. 12). It can be seen that the changes of the depth location of the peak AE source density were considerably minor. In addition, the curves with respect to different penetration depth shared very similar shape. It is

therefore again indicated that the target AE source area was pushed downward together with the advancing pile tip.

Fig. 13 summarizes the depth positions of the ground with maximum AE source density. It is clearly illustrated that the absolute depth of AE source concentration zone increased with the pile penetration depth, demonstrating the evolving of the AE source position. On the other hand, the relative distance of this zone to the real time pile tip showed different trends. During the 1st load, the cluster of AE sources was generally moving away from the pile tip,

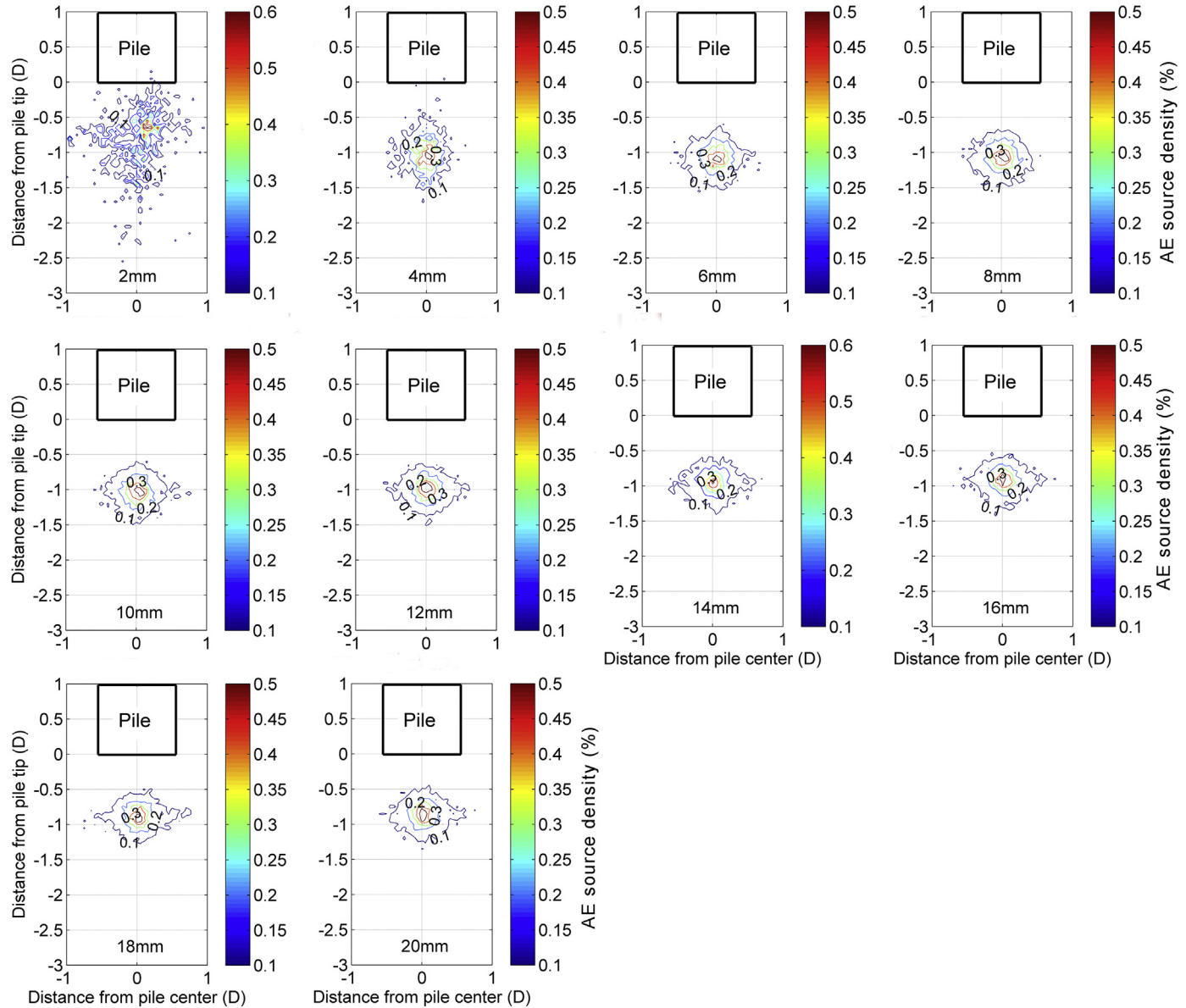


**Fig. 9.** Contour distribution of AE sources: 1st load.

while during the 2nd load, it gradually moved upward approaching the pile tip.

## 5. Particle breakage observation

The results of AE source location suggested that the zone of particle breakage is not uniformly distributed below the pile tip, but restricted to a small area. By roughly retrieving the sand of different depths below the pile tip, it is clearly confirmed that the sand located within 20–30 mm below the pile tip suffered higher degree of breakage than that from 0 to 10 mm, as shown in Fig. 14.

In order to have closer observations of particle breakage, additional tests were performed for posttest excavations. For better visual discrimination, the sands of same material but with larger size ( $D_{50} = 1.7$  mm) were used. After the pile penetration, the pile was fixed to the installation footing to hold still. Then, the sands in the model ground were removed carefully until reaching the pile tip. Finally, the pile was removed from the installation footing and

the sands below the pile tip were exposed. The additional stress or disturbance to the target sands throughout the whole excavation process was controlled to a minimum level so that no additional particle breakage would be produced during this process. Afterwards, the images were taken by a microscope camera at different depths after removing the sands layer by layer.

Fig. 15 shows the photos of a typical result when the ground excavation reaches the pile tip. The crushed fines (white color) are seen surrounding the pile edge (Fig. 15a). When the pile is removed, however, it is seen that the breakage is not evident for the sands inside the circular pile edge (Fig. 15b). Microscopic images for particle breakage observation along the pile center profile at different depth are shown in Fig. 16. It is found that little particle breakage could be noticed immediately beneath the pile tip, while the severest breakage zone appeared at ~20–35 mm below the pile tip. For sand located more than 45 mm below the pile tip, the breakage became insignificant again. Such observation agrees well with the AE source distributions shown in Figs. 10 and 12, where

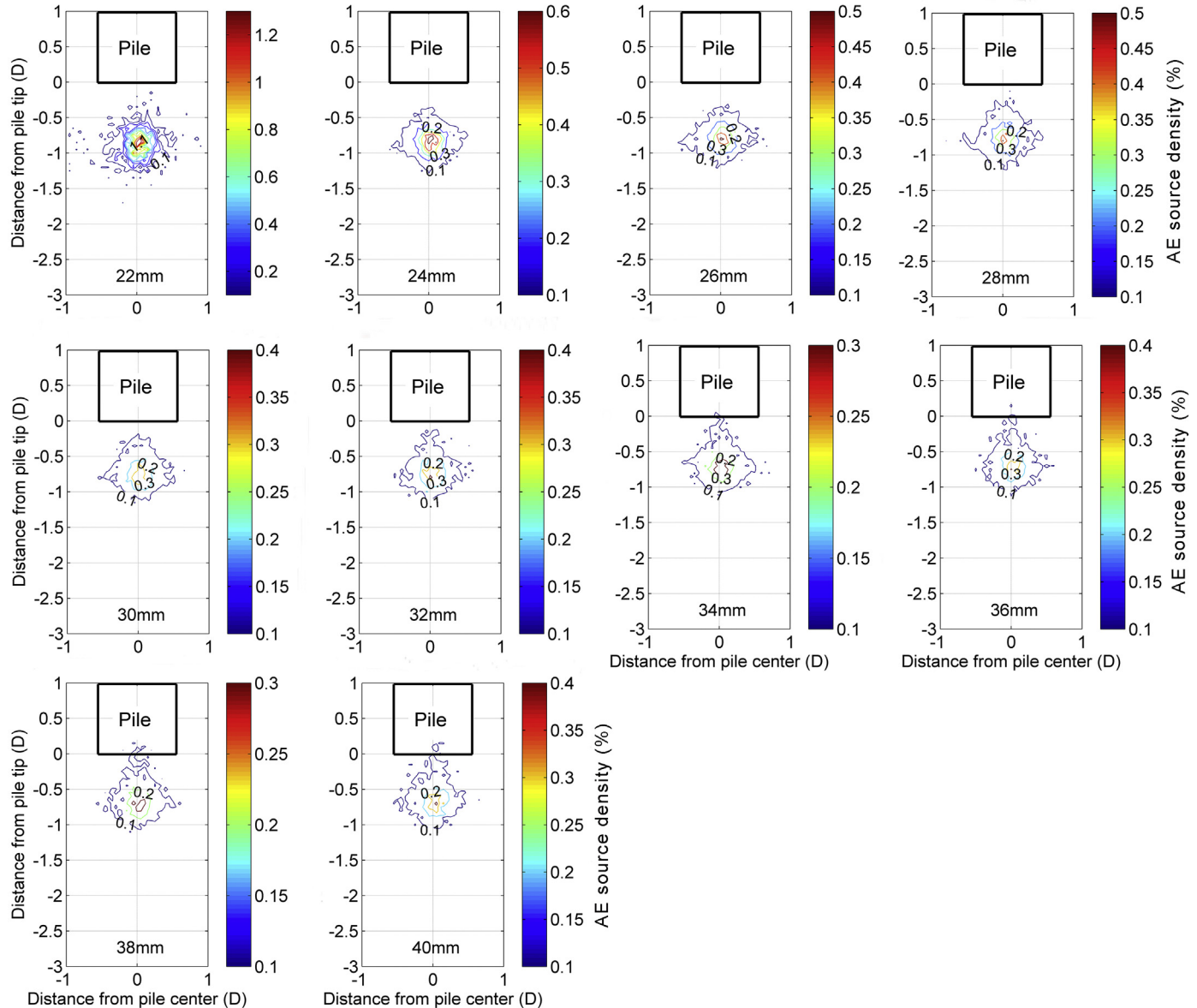


**Fig. 10.** Contour distribution of AE sources: 2nd load.

maximum AE source density was found to be located  $0.5D$ – $1D$  after 40 mm penetration.

The observation of particle breakage adjacent to the pile tip was also performed by Yang et al. (2010), where the crushed fines were found to be adhered to the pile shaft near the pile tip. This observation is similar with the current study as shown in Fig. 15. The pile edge was surrounded by the crushed fines. Yang et al. (2010) further classified the breakage zone below the pile tip into three zones based on the stress conditions of each zone. The soils in the shear band subjected to extreme normal and shear stress underwent the severest breakage, followed by the non-shear band zone with high normal stress (significant breakage) and reduced normal stress (moderate breakage). Due to the cone-shaped pile end, the breakage status of sand immediately below a flat ended pile was not observed.

The flat-ended pile was adopted by White and Bolton (2004) in the plane-strain calibration chamber test for PIV (Particle Image Velocimetry) analysis of the ground deformation. They reported a

“nose cone” shaped breakage zone below the pile tip through a transparent observation window. This seems to be different from the current test results. However, it should be noted that the PIV method traces the trajectories of the soil patch based on the ratio of matching between sequential images. When the soil is subjected to breakage, the PIV method fails to function well since the original searching patch no longer exists. In addition, the scratching between pile surface and the observation window, as well as the sand penetration in the gap would add errors to the PIV analyses. Fig. 17 illustrates the deterioration of observation conditions in an additionally performed PIV testing setup. The details of this PIV testing arrangement can be referred to Aoyama et al. (2016), and the analysis method is the same with White and Bolton (2004). It is clearly shown in Fig. 17 that the sands penetrated into the gap between the pile and the wall interface and there are crushed fines (white color) immediately below the pile tip due to interface scratching. Therefore, the resultant “nose cone” of particle breakage should be mainly attributed to the interface shearing of the sands in

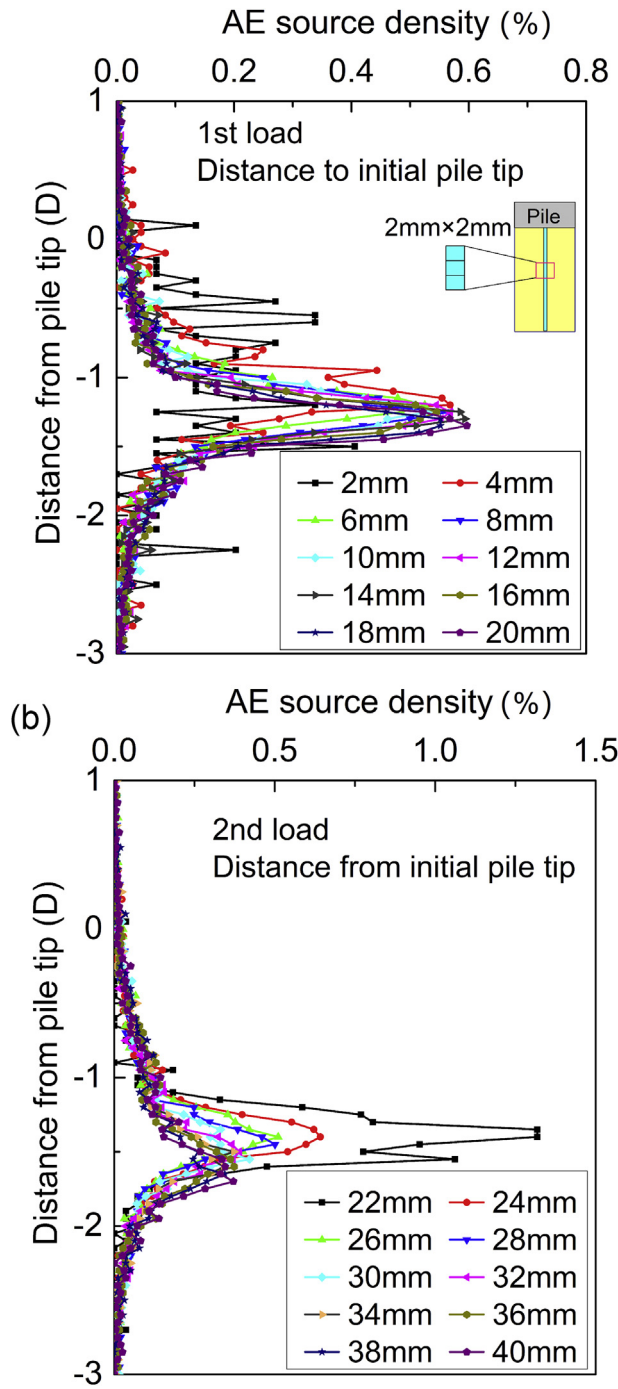
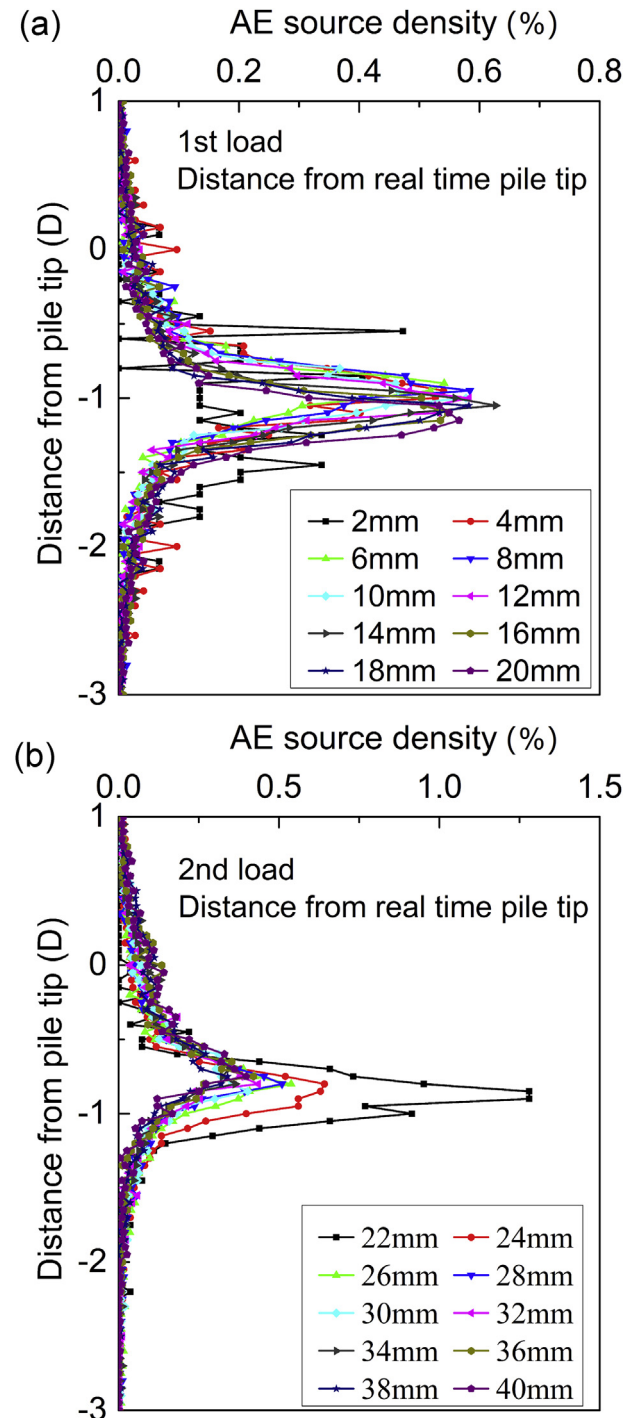


**Fig. 11.** Density distribution of AE sources along the profile of pile center with pile end position fixed at initial depth (data retrieved in  $2 \text{ mm} \times 2 \text{ mm}$  sub-patches). (a) 1st load; (b) 2nd load.

the gap between pile and observation window, or the scratching between sands and observation window, which is different from particle breakage mechanism under three dimensional stress conditions.

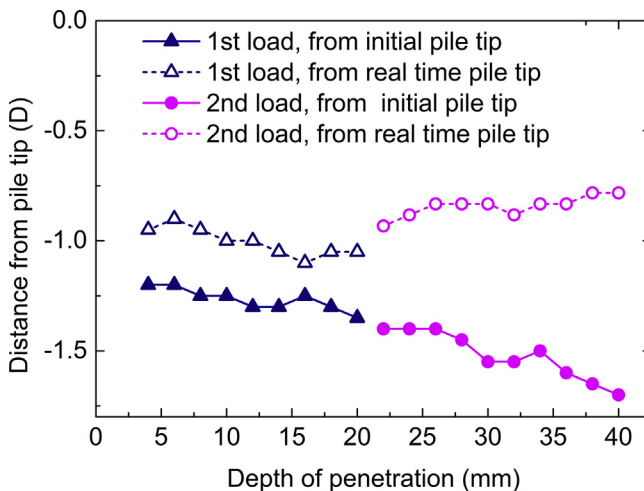
#### 6. Ground deformation and evolution of particle breakage zone

Fig. 18 shows a typical vertical profile of subsoil after pile penetration by using color sands to mark the ground deformation.



**Fig. 12.** Density distribution of AE sources along the profile of pile center with source depth modified with real time pile end position. (a) 1st load; (b) 2nd load.

It is clearly demonstrated that the soils immediate below the pile tip are pushed downward after pile penetration. The ground deformation can be well captured though PIV analysis, as shown in Fig. 19. Detailed descriptions of the PIV testing procedures can be referred to Aoyama et al. (2016), and the theoretical background should be referred to White et al. (2001, 2003) and White and Bolton (2004). Fig. 19a shows a typical vector displacement field around the pile tip, which is combined by a vertical displacement field shown in Fig. 19b and a horizontal displacement field shown in



**Fig. 13.** Depth evolution of spatial location with maximum AE source density.

**Fig. 19c.** For sands immediately below the pile tip, the value of the vertical displacement is close to the pile penetration depth (i.e. 1 mm in the current case). In the horizontal direction, the ground deformation is approximately symmetric along the pile center profile. That is, the subsoil is deformed toward the two sides when the pile is approaching from above. It should be noted that the horizontal displacement is considerably small within the region immediately below the pile tip where vertical displacement is evident. The incremental shear strain fields derived from the displacement field are displayed in **Fig. 19d, e** in the forms of engineering shear strain and maximum shear strain. The definition and the computation details can be referred to [White and Bolton \(2004\)](#). Similar with the horizontal displacement field, it is seen that the shear strain is developed in two opposite directions and mainly concentrated near the pile edge. Overall, the maximum shear strain is restricted to a limited region below the pile tip, with the values decreased as the distance from the pile tip increased. The characteristics of the ground deformation as well as the strain distributions demonstrate that the subsoil is moving downward together with the advancing pile, while the shear zone is developed close to the pile tip. This is consistent with the results of AE source location as well as soil profile shown in **Fig. 18**.

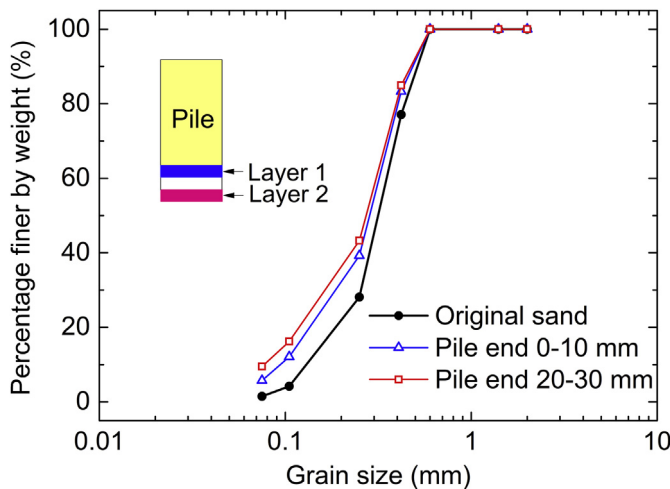


**Fig. 14.** Grain size distributions of the sand retrieved from different depths below pile tip.



**Fig. 15.** Photos taken after removing the sand above pile tip. (a) With pile; (b) pile removed.

The process of pile penetration is analogous to that of the soil streams passing through a stationary pile as described by [White and Bolton \(2004\)](#). The path of sand stream formed the shear zone around the pile shaft where severest particle breakage occurred as observed by [Yang et al. \(2010\)](#) and as shown in **Fig. 16** in the current study. Regarding a flat-ended pile, the soils immediate below the pile tip, marked as Zone 1 in **Fig. 20**, are approximately subjected to the triaxial compression condition, while the soils located in the shear zone, marked as Zone 2 in **Fig. 20**, are subjected to large shear deformation condition, which is also evidenced by the shear strain field shown in **Fig. 19d, e**. Previous studies have both experimentally and numerically proved that particle breakage occurs more easily under shear than compression ([Lee and Coop, 1995](#); [Ovalle et al., 2015](#); [Ma et al., 2016, 2018](#); [Yu, 2017c](#)). Moreover, [Sadrekarimi and Olson \(2010\)](#) reported that particle breakage can be observed even when normal stress is very small during ring shear test. In the current study, the maximum ground resistance measured by the strain gauges attached near the pile tip was about 10 kN, yielding the normal stress below the pile tip to be approximately 8 MPa considering the pile bottom area, which is much lower than the stress value (ca. 20 MPa in silica sand) that noticeable amount of particle breakage is expected in a compression condition according to the high pressure one dimensional compression tests ([Hagerty et al., 1993](#); [Yamamoto et al., 1996](#); [Nakata et al., 2001](#); [Cil and Alshibli, 2014](#)). It is therefore suggested that the shear zone is responsible for the significant particle breakage observed.

On the other hand, however, although Zone 1 exhibited no noticeable particle breakage in the current study, substantial particle breakage can still occur at high pressures based on previous

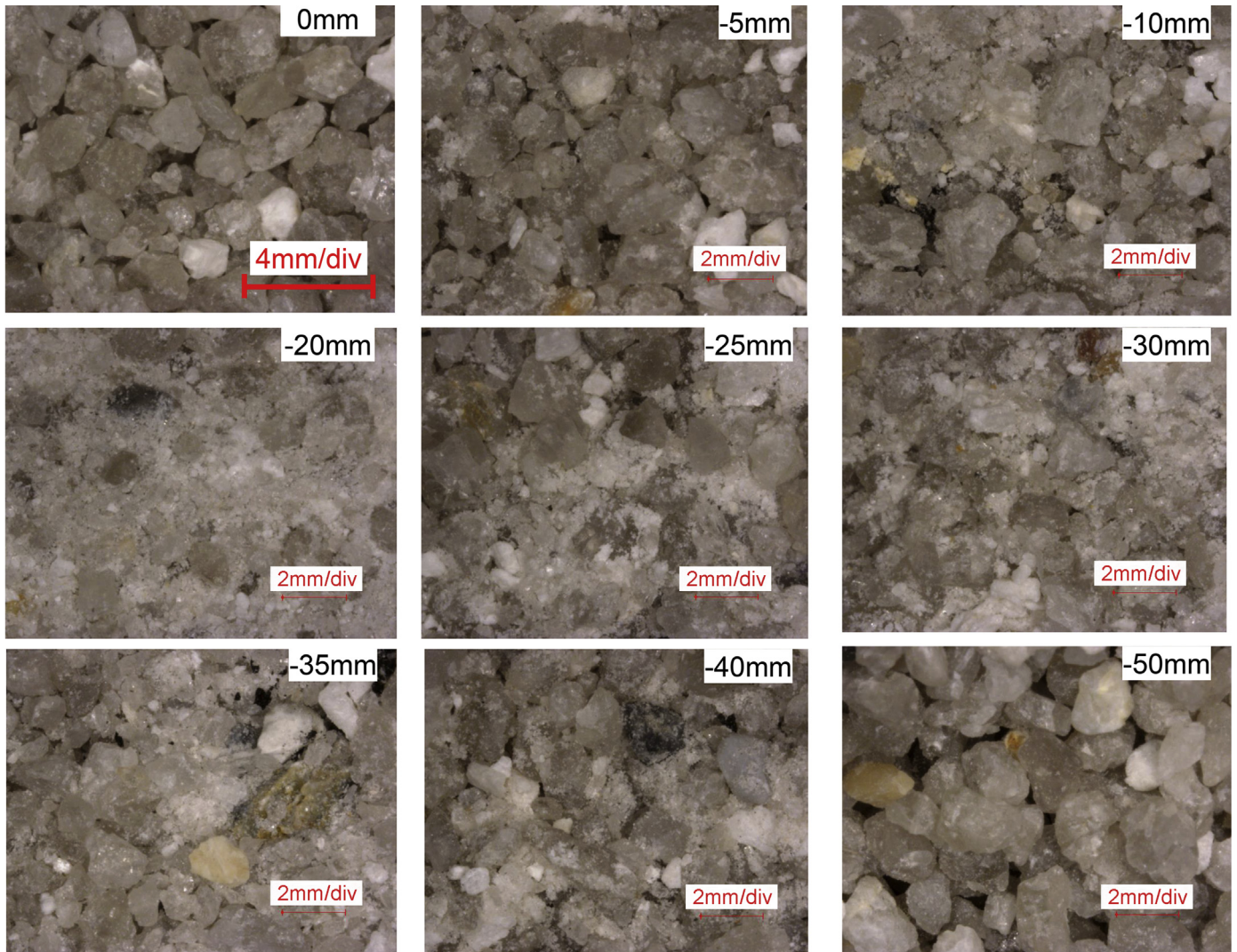


**Fig. 16.** Microscopic observation of particle breakage through posttest excavation.

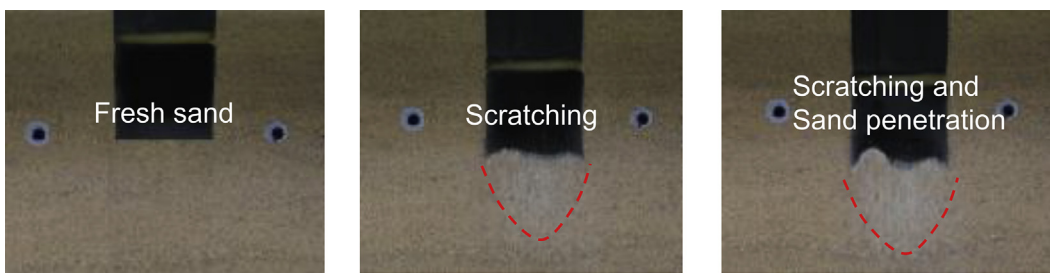


**Fig. 17.** Deterioration of observation conditions for PIV analysis in a 2-dimensional testing situation.

studies (Hagerty et al., 1993; Yamamuro et al., 1996; Nakata et al., 2001; Cil and Alshibli, 2014). It is therefore suggested that Zone 1 may disappear when the ground bearing pressure is large enough. Besides, Zone 1 is subjected to shrink with the process of pile penetration. In view of sand stream, Zone 1 may shrink due to continuous erosion of the shear zone during pile advancing. This can be verified through the results of AE source location as summarized in Fig. 13. The position of location with maximum AE source density kept moving toward the pile tip during the 2nd pile

penetration, demonstrating the shrinking of Zone 1. In addition, the soils located in Zone 1 had the tendency of extension in the horizontal direction since the vertical stress is larger than the horizontal stress. This could also accelerate the erosion of soils near the boundary of the shear zone. Nevertheless, considering shear failure is more likely to occur in the case of pile foundation, it is more important to concern particle breakage within the shear zone when dealing with particle breakage issues.



Fig. 18. Vertical profile demonstrating subsoil deformation.

## 7. Advantage and limitations of the AE monitoring method

As a non-destructive testing method, the AE source location provides direct information of the ground conditions, which allows a unique insight into the particle breakage behavior regarding pile penetration process. In the current study, the AE sources were found to be not uniformly distributed, but concentrated within a limited area at certain depth below the pile tip, which corresponded well with the zone of particle breakage after posttest observation. In addition, the evolution of spatial distributions of AE

sources represented the evolution process of the breakage zone in a three dimensional manner, which is helpful for further understanding of the particle breakage mechanism.

On the other hand, it should be noted that there exists certain drawbacks for the application of AE method for monitoring of porous soil material. The main problem involved here is the considerable attenuation of elastic waves in the soil. This issue is particularly critical for the particle breakage problem. Experimental evidences suggested that particle breakage is usually accompanied by AE signals with high frequency component (Mao and Towhata, 2015; Mao et al., 2018b). Therefore, a threshold of 100 kHz of the dominant frequency of a signal was used to discriminate the AE signals from different source mechanisms, i.e. particle sliding and breakage. This is quite useful and effective when the interpretation of results is based on signal energy or count number, since such parameters will not change significantly when the signal is applied to spectrum analysis. However, when dealing with source location issue, the accurate arrival time of a signal is required and this can be affected if the signal is further treated. In addition, high frequency component can be easily attenuated in a granular system and this could lead to inaccurate arrival time determination, because the amplitude of a signal near the point of signal arrival is low and can be easily drowned in the background noise. Therefore, in the current study, the results are presented using the original captured signals without any further treatment to separate high frequency components.

In addition, the source of AE signals generated in the stressed soils has different characteristics from those in rock or concrete materials. For soils, the AE signals can be generated due to

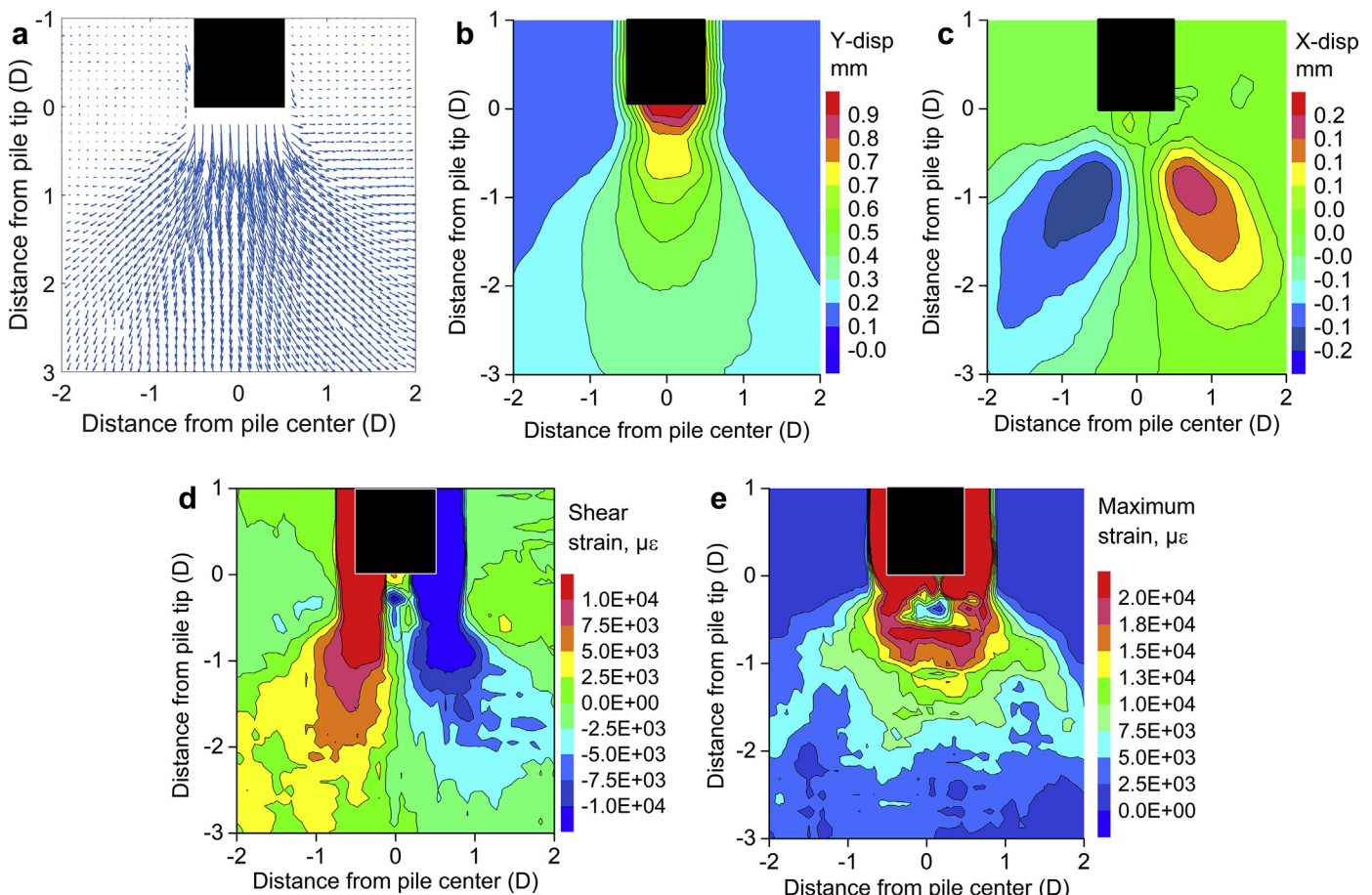
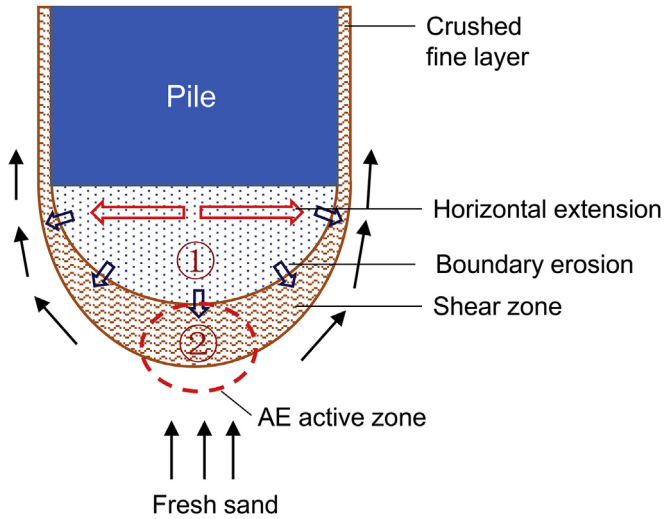


Fig. 19. Displacement field around a pile tip (9–13 mm penetration). (a) Vector plot; (b) vertical displacement; (c) horizontal displacement; (d) shear strain; (e) maximum strain.



**Fig. 20.** Schematic illustration of particle breakage zone.

numerous contacts between particles. Consequently, events with lower amplitudes are easily submerged by those with higher amplitudes occurred simultaneously. As a result, the AE sources localized from stressed soils have the bias to reveal the most “noisy” zone. In the current study, it corresponds to the shear zone right under the pile tip where the direction of soil flow changed most sharply when the pile approaching from above (indicated by dashed circle in Fig. 20).

So far, the measuring of GSD before and after a test is the most common method for evaluation of particle breakage behavior. As a non-destructive method, the AE monitoring offers an alternative way for real time investigation of particle breakage, which is a useful supplement to the traditional research methods. Considering the complexity of particle breakage problem, a combination of the relevant testing methodology should be applied in order to realize a comprehensive understanding on the particle breakage behavior.

## 8. Conclusions

This study presents an AE source localization method for investigation of particle breakage during pile penetration process. The main findings are summarized as follows:

- (1) The AE sources are concentrated within certain zones, usually around  $0.5D$ – $1D$  below the pile tip. This AE concentration zone is pushed downward with the advancing pile tip, and its distance to the real time pile tip decreased after certain depth of pile penetration.
- (2) Posttest excavation showed that the sand in the shear zone experienced the severest breakage, while the sand in the compression zone immediately below pile tip had insignificant breakage.
- (3) The most active area of AE source corresponds to the tip of cone shaped area of the shear zone below the pile tip. This is possibly attributed to the fact that the subsoil deformed toward the two opposite sides when the pile above is approaching, as revealed by the PIV analysis.
- (4) The compression zone with insignificant particle breakage in the current study may shrink or even disappear when the ground bearing pressure is large enough, or due to continuous erosion of the shear zone during pile penetration.

## Acknowledgement

This study is sponsored by the Shanghai Sailing Program (Grant No. 18YF1424000), and Shanghai Education Commission (Peak Discipline Construction Program, Grant Nos. 0200121005/052 & 2019010206). The authors are grateful to Professor Junichi Koseki of the University of Tokyo for his valuable advice on this work. PIV program used in this study was provided by Prof. David J. White of University of Western Australia. These assistances are greatly acknowledged by the authors.

## Appendix. Brief derivation of the AR-AIC model

The general form of an autoregressive model for a time series  $X_t = [X_1, \dots, X_t]$  can be written as (Takanami and Kitagawa, 1988; Niccolini et al., 2012):

$$X_t = c + \sum_{i=1}^p \varphi_i X_{t-i} + \varepsilon_t \quad (\text{A1})$$

where  $c$  is constant value;  $\varphi_i$  ( $i = 1, 2, 3, \dots, p$ ) is the coefficient of the AR model;  $\varepsilon_t$  is white noise;  $p$  is order of the AR model.

Suppose  $\{X_1, X_2, X_3, \dots, X_N\}$  is a digitalized signal obtained from the sensor, containing both background noise and the signal part. Therefore, this time series can be divided into two segments: the noise part  $\{X_1, X_2, X_3, \dots, X_M\}$ , and the signal part  $\{X_{M+1}, X_{M+2}, X_{M+3}, \dots, X_N\}$ , where  $M$  here identifies the unknown signal onset. Accordingly, each of the two intervals is modeled as an autoregressive process of order  $p^n$  with coefficients  $a_j^n$  ( $i = n, s$  corresponding to the noise and signal part respectively).

For the noise part AR ( $p^n$ ):

$$x_m^n = \sum_{j=1}^{p^n} a_j^n x_{m-j} + \varepsilon_n^n \quad (\text{A2})$$

where  $m = 1, 2, 3, \dots, M$ .  $p^n$  is the order of the noise part AR model.  $a_j^n$  is the autoregressive coefficient, and  $\varepsilon_n^n$  is the white noise (mean = 0, variance =  $\sigma_n^2$ ).

For signal part AR ( $p^s$ ):

$$x_m^s = \sum_{j=1}^{p^s} a_j^s x_{m-j} + \varepsilon_n^s \quad (\text{A3})$$

where  $m = M+1, M+2, M+3, \dots, N$ .  $p^s$  is the order of the signal part AR model.  $a_j^s$  is the autoregressive coefficient, and  $\varepsilon_n^s$  is the white noise (mean = 0, variance =  $\sigma_s^2$ ).

Taking noise part for example, Eq. (A2) can be rewritten as:

$$\mathbf{Y}^n = \mathbf{X}^n \mathbf{a}^n + \boldsymbol{\varepsilon}^n \quad (\text{A4})$$

where

$$\mathbf{Y}^n = [x_{p^n+1} \ x_{p^n+2} \ x_{p^n+3} \ \dots \ x_{p^n+M}] \quad (\text{A5})$$

$$\mathbf{a}^n = [a_1 \ a_2 \ a_3 \ \dots \ a_M]^T \quad (\text{A6})$$

$$\boldsymbol{\varepsilon}^n = [\varepsilon_1 \ \varepsilon_2 \ \varepsilon_3 \ \dots \ \varepsilon_M]^T \quad (\text{A7})$$

$$\mathbf{X}^n = \begin{bmatrix} x_{p^n} & x_{p^n-1} & \dots & x_1 \\ x_{p^n+1} & x_{p^n} & \dots & x_2 \\ \dots & \dots & \dots & \dots \\ x_{M-1} & x_{M-2} & \dots & x_{M-p^n} \end{bmatrix} \quad (\text{A8})$$

By applying the least square method (Cheung et al., 2004),  $\mathbf{a}^n$  can be estimated as

$$\mathbf{a}^n = (\mathbf{X}^{nT} \mathbf{X}^n)^{-1} \mathbf{X}^{nT} \mathbf{Y}^n \quad (A9)$$

Therefore, the variance  $\sigma_{n, max}^2$  is

$$\sigma_{n, max}^2 = \frac{(\mathbf{Y}^n - \mathbf{X}^n \mathbf{a}^n)^T (\mathbf{Y}^n - \mathbf{X}^n \mathbf{a}^n)}{M - p^n} \quad (A10)$$

The AIC value of the noise part is given by the equation below (Takanami and Kitagawa, 1988; Niccolini et al., 2012).

$$AIC_{\text{noise}} = M \log(\sigma_{n, max}^2) + 2p^n \quad (A11)$$

Being similar to the noise part, the  $\sigma_{s, max}^2$  of the signal part can also be obtained. Consequently, the AIC of the whole calculation window is derived:

$$AIC_{\text{total}} = AIC_{\text{signal}} + AIC_{\text{noise}} \quad (A12)$$

The arrival time of the signal corresponds to the minimum AIC value of the whole signal window derived from Eq. (A12) (Akaike, 1973).

## References

- Akaike, H., 1973. Information theory and an extension of the maximum likelihood principle. In: 2nd International Symposium on Information Theory. Academiai Kiado.
- Al-Balushi, K.R., Addali, A., Charnley, B., Mba, D., 2010. Energy Index technique for detection of acoustic emissions associated with incipient bearing failures. *Applied Acoustics* 71 (9), 812–821.
- Altuhafi, F.N., Jardine, R.J., Georgiannou, V.N., Moinet, W.W., 2017. Effects of particle breakage and stress reversal on the behaviour of sand around displacement piles. *Géotechnique* 68 (6), 546–555.
- Aoyama, S., Mao, W., Goto, S., Towhata, I., 2016. Application of advanced procedures to model tests on the subsoil behavior under vertical loading of group pile in sand. *Indian Geotechnical Journal* 46 (1), 64–76.
- Bandini, V., Coop, M.R., 2011. The influence of particle breakage on the location of the critical state line of sands. *Soils and Foundations* 51 (4), 591–600.
- Butterfield, J.D., Krynnik, A., Collins, R.P., Beck, S.B.M., 2017. Experimental investigation into vibro-acoustic emission signal processing techniques to quantify leak flow rate in plastic water distribution pipes. *Applied Acoustics* 119, 146–155.
- Carpinteri, A., Lacidogna, G., Pugno, N., 2007. Structural damage diagnosis and life-time assessment by acoustic emission monitoring. *Engineering Fracture Mechanics* 74 (1–2), 273–289.
- Cheung, K.W., So, H.C., Ma, W.K., Chan, Y.T., 2004. Least squares algorithms for time-of-arrival-based mobile location. *IEEE Transactions on Signal Processing* 52 (4), 1121–1130.
- Cil, M.B., Alshibli, K.A., 2014. 3D evolution of sand fracture under 1D compression. *Géotechnique* 64 (5), 351–364.
- Dong, L.J., Li, X.B., Zhou, Z.L., Chen, G.H., Ju, M.A., 2015. Three-dimensional analytical solution of acoustic emission source location for cuboid monitoring network without pre-measured wave velocity. *Transactions of Nonferrous Metals Society of China* 25 (1), 293–302.
- Eaton, M.J., Pullin, R., Holford, K.M., 2012. Acoustic emission source location in composite materials using Delta T Mapping. *Composites Part A: Applied Science and Manufacturing* 43 (6), 856–863.
- Einav, I., 2007. Breakage mechanics—part I: theory. *Journal of the Mechanics and Physics of Solids* 55 (6), 1274–1297.
- Eskişar, T., Otani, J., Hironaka, J., 2012. Visualization of soil arching on reinforced embankment with rigid pile foundation using X-ray CT. *Geotextiles and Geomembranes* 32, 44–54.
- Filippov, A.V., Rubtsov, V.E., Tarasov, S.Y., 2017. Acoustic emission study of surface deterioration in tribocorrosion. *Applied Acoustics* 117, 106–112.
- Ghafghazi, M., Shuttle, D.A., DeJong, J.T., 2014. Particle breakage and the critical state of sand. *Soils and Foundations* 54 (3), 451–461.
- Gutkin, R., Green, C.J., Vangrattanachai, S., Pinho, S.T., Robinson, P., Curtis, P.T., 2011. On acoustic emission for failure investigation in CFRP: pattern recognition and peak frequency analyses. *Mechanical Systems and Signal Processing* 25 (4), 1393–1407.
- Hagerty, M.M., Hite, D.R., Ullrich, C.R., Hagerty, D.J., 1993. One-dimensional high-pressure compression of granular media. *Journal of Geotechnical Engineering* 119 (1), 1–18.
- He, M.C., Miao, J.L., Feng, J.L., 2010. Rock burst process of limestone and its acoustic emission characteristics under true-triaxial unloading conditions. *International Journal of Rock Mechanics and Mining Sciences* 47 (2), 286–298.
- Hu, W., Yin, Z., Dano, C., Hicher, P.Y., 2011. A constitutive model for granular materials considering grain breakage. *Science China Technological Sciences* 54 (8), 2188–2196.
- Huang, W., Zhang, W., Li, F., 2013. Acoustic emission source location using a distributed feedback fiber laser rosette. *Sensors* 13 (10), 14041–14054.
- Imre, B., Laue, J., Springman, S.M., 2010. Fractal fragmentation of rocks within sturzstroms: insight derived from physical experiments within the ETH geotechnical drum centrifuge. *Granular Matter* 12 (3), 267–285.
- Indraratna, B., Wadud, S., Rujikiatkamjorn, C., 2007. Development and application of constitutive model for railway ballast. In: Yin, J.H., Li, X.S., Yeung, A.T., Desai, C.S. (Eds.), *International Workshop on Constitutive Modelling*, Hong Kong, January, 2007, pp. 685–696.
- Jardine, R.J., Zhu, B.T., Foray, P., Yang, Z.X., 2013a. Interpretation of stress measurements made around closed-ended displacement piles in sand. *Géotechnique* 63 (8), 613–627.
- Jardine, R.J., Zhu, B., Foray, P., Yang, Z.X., 2013b. Measurement of stresses around closed-ended displacement piles in sand. *Géotechnique* 63 (1), 1–17.
- Kundu, T., 2014. Acoustic source localization. *Ultrasonics* 54 (1), 25–38.
- Kuwajima, K., Hyodo, M., Hyde, A.F., 2009. Pile bearing capacity factors and soil crushability. *Journal of Geotechnical and Geoenvironmental Engineering* 135 (7), 901–913.
- Lee, I.K., Coop, M.R., 1995. The intrinsic behaviour of a decomposed granite soil. *Géotechnique* 45 (1), 117–130.
- Lobo-Guerrero, S., Vallejo, L.E., 2005. DEM analysis of crushing around driven piles in granular materials. *Géotechnique* 55 (8).
- Ma, G., Regueiro, R.A., Zhou, W., Wang, Q., Liu, J., 2018. Role of particle crushing on particle kinematics and shear banding in granular materials. *Acta Geotechnica* 13 (3), 601–618.
- Ma, G., Zhou, W., Chang, X.L., Ng, T.T., Yang, L.F., 2016. Formation of shear bands in crushable and irregularly shaped granular materials and the associated microstructural evolution. *Powder Technology* 301, 118–130.
- Mao, W., Aoyama, S., Towhata, I., 2015. Acoustic emission characteristics of subsoil subjected to vertical pile loading in sand. *Journal of Applied Geophysics* 119, 119–127.
- Mao, W., Aoyama, S., Towhata, I., 2018a. Feasibility study of using acoustic emission signals for investigation of pile spacing effect on group pile behavior. *Applied Acoustics* 139, 189–202.
- Mao, W., Yang, Y., Lin, W., Aoyama, S., Towhata, I., 2018b. High frequency acoustic emissions observed during model pile penetration in sand and implications for particle breakage behavior. *International Journal of Geomechanics* 18 (11), 04018143.
- Mao, W., Towhata, I., 2015. Monitoring of single-particle fragmentation process under static loading using acoustic emission. *Applied Acoustics* 94, 39–45.
- McDowell, G.R., Bolton, M.D., 2000. Effect of particle size distribution on pile tip resistance in calcareous sand in the geotechnical centrifuge. *Granular Matter* 2 (4), 179–187.
- Murff, J.D., 1987. Pile capacity in calcareous sands: state of the art. *Journal of Geotechnical Engineering* 113 (5), 490–507.
- Nakata, Y., Kato, Y., Hyodo, M., Hyde, A.F., Murata, H., 2001. One-dimensional compression behavior of uniformly graded sand related to single particle crushing strength. *Soils and Foundations* 41 (2), 39–51.
- Niccolini, G., Xu, J., Manuello, A., Lacidogna, G., Carpinteri, A., 2012. Onset time determination of acoustic and electromagnetic emission during rock fracture. *Progress in Electromagnetics Research Letters* 35, 51–62.
- Ovalle, C., Dano, C., Hicher, P.Y., Cisternas, M., 2015. Experimental framework for evaluating the mechanical behavior of dry and wet crushable granular materials based on the particle breakage ratio. *Canadian Geotechnical Journal* 52 (5), 587–599.
- Randolph, M.F., 2003. Science and empiricism in pile foundation design. *Géotechnique* 53 (10), 847–875.
- Roberts, T., Talebzadeh, M., 2003. Acoustic emission monitoring of fatigue crack propagation. *Journal of Constructional Steel Research* 59 (6), 695–712.
- Sadrekarimi, A., 2012. Effect of soil particle mineralogy on embankment dams. *Proceedings of the ICE - Geotechnical Engineering* 165 (3), 195–206.
- Sadrekarimi, A., Olson, S.M., 2010. Particle damage observed in ring shear tests on sands. *Canadian Geotechnical Journal* 47 (5), 497–515.
- Salim, W., Indraratna, B., 2004. A new elastoplastic constitutive model for coarse granular aggregates incorporating particle breakage. *Canadian Geotechnical Journal* 41 (4), 657–671.
- Shiotani, T., 2006. Evaluation of long-term stability for rock slope by means of acoustic emission technique. *NDT & E International* 39 (3), 217–228.
- Simonini, P., 1996. Analysis of behavior of sand surrounding pile tips. *Journal of Geotechnical Engineering* 122 (11), 897–905.
- Takanami, T., Kitagawa, G., 1988. A new efficient procedure for the estimation of onset times of seismic waves. *Journal of Physics of the Earth* 36 (6), 267–290.
- Ueng, T.S., Chen, T.J., 2000. Energy aspects of particle breakage in drained shear of sands. *Géotechnique* 50 (1), 65–72.
- White, D.J., Bolton, M.D., 2004. Displacement and strain paths during plane strain model pile installation in sand. *Géotechnique* 54 (6), 375–397.
- White, D.J., Take, W.A., Bolton, M.D., 2001. Measuring soil deformation in geotechnical models using digital images and PIV analysis. *Proc. 10th Int. Conf. Computer Methods and Advances in Geomechanics* 997–1002.

- White, D.J., Take, W.A., Bolton, M.D., 2003. Soil deformation measurement using particle image velocimetry (PIV) and photogrammetry. *Géotechnique* 53 (7), 619–631.
- Xiao, Y., Liu, H., 2017. Elastoplastic constitutive model for rockfill materials considering particle breakage. *International Journal of Geomechanics* 17 (1), 04016041.
- Xiao, Y., Liu, H., Desai, C.S., Sun, Y., Liu, H., 2015a. Effect of intermediate principal-stress ratio on particle breakage of rockfill material. *Journal of Geotechnical and Geoenvironmental Engineering* 142 (4), 06015017.
- Xiao, Y., Liu, H., Ding, X., Chen, Y., Jiang, J., Zhang, W., 2015b. Influence of particle breakage on critical state line of rockfill material. *International Journal of Geomechanics* 16 (1), 04015031.
- Xiao, Y., Meng, M., Daoudjia, A., Chen, Q., Wu, Z., Jiang, X., 2018a. Effect of particle size on crushing and deformation behaviors of rockfill materials. *Geoscience Frontiers*. <https://doi.org/10.1016/j.gsf.2018.10.010> (This issue).
- Xiao, Y., Stuedlein, A.W., Chen, Q., Liu, H., Liu, P., 2017. Stress-strain-strength response and ductility of gravels improved by polyurethane foam adhesive. *Journal of Geotechnical and Geoenvironmental Engineering* 144 (2), 04017108.
- Xiao, Y., Sun, Z., Stuedlein, A.W., Wang, C., Wu, Z., Zhang, Z., 2018b. Bounding surface plasticity model for stress-strain and grain crushing behaviors of rockfill materials. *Geoscience Frontiers*. <https://doi.org/10.1016/j.gsf.2019.06.010> (This issue).
- Yamamoto, J.A., Bopp, P.A., Lade, P.V., 1996. One-dimensional compression of sands at high pressures. *Journal of Geotechnical Engineering* 122 (2), 147–154.
- Yang, J., 2006. Influence zone for end bearing of piles in sand. *Journal of Geotechnical and Geoenvironmental Engineering* 132 (9), 1229–1237.
- Yang, Z.X., Jardine, R.J., Zhu, B.T., Foray, P., Tsuha, C.H.C., 2010. Sand grain crushing and interface shearing during displacement pile installation in sand. *Géotechnique* 60 (6), 469.
- Yasufuku, N., Hyde, A.F.L., 1995. Pile end-bearing capacity in crushable sands. *Géotechnique* 45 (4), 663–676.
- Yasufuku, N., Ochiai, H., Ohno, S., 2001. Pile end-bearing capacity of sand related to soil compressibility. *Soils and Foundations* 41 (4), 59–71.
- Yu, F., 2017a. Characteristics of particle breakage of sand in triaxial shear. *Powder Technology* 320, 656–667.
- Yu, F., 2017b. Particle breakage and the critical state of sands. *Géotechnique* 67 (8), 713–719.
- Yu, F., 2017c. Particle breakage and the drained shear behavior of sands. *International Journal of Geomechanics* 17 (8), 04017041.
- Zhang, C., Nguyen, G.D., Einav, I., 2013. The end-bearing capacity of piles penetrating into crushable soils. *Géotechnique* 63 (5), 341–354.
- Zhang, C., Yang, Z.X., Nguyen, G.D., Jardine, R.J., Einav, I., 2014. Theoretical breakage mechanics and experimental assessment of stresses surrounding piles penetrating into dense silica sand. *Géotechnique Letters* 4 (1), 11–16.